Modelling 3D anisotropic elastic data using the pseudospectral approach

Richard A. Bale

ABSTRACT

A method is described for modelling 3D elastic data in anisotropic media, based on the pseudospectral approach. The goal is to model the effects of azimuthal anisotropy on 3D shear-wave data, in particular the phenomenon of shear-wave splitting. The pseudospectral approach is used in preference to other gridded methods on efficiency grounds, because of its economy in the number of grid points required. Numerical issues, including dispersion, boundary effects and non-local operator artifacts are discussed, and solutions to them are provided. A comparison with the analytic result for a displacement source in a homogeneous medium shows the high accuracy of elastic pseudospectral modelling. Preliminary results of modelling in 2D and 3D anisotropic models are presented and analyzed. The expected shear-wave behaviour is observed in simple cases. This pseudospectral modelling technique is suitable for testing multicomponent processing or imaging algorithms in the presence of anisotropy.

INTRODUCTION

Numerical modelling has a long and well established role in geophysical analysis. When selecting a numerical modelling technique, the geophysicist should ask: "What is my purpose in modelling, and how does that influence the choice of algorithm?" The theory of modelling, whether ray-tracing, finite-difference or pseudospectral, is a rich mixture of wave theory, numerical techniques and computer science. Thus, one possible motive (quite legitimate in my view) is the intrinsic interest of the theory. More typically, the goal will be to create synthetic seismic data, enabling us to better understand real data, and to test imaging or processing methods.

My objective here is to model elastic behaviour in 3D azimuthally anisotropic media. More specifically, it is to be able to simulate shear-wave splitting in realistic cases: e.g. multicomponent surveys over azimuthally anisotropic rocks, such as fractured reservoirs. Shear-waves are especially sensitive to fractures, which cause two separate polarizations of the shear-waves. This phenomenon, known as shear-wave splitting or "birefringence", is useful for determining the fracture directions and intensity. Li (1998) observed that 3D converted wave data are especially useful for fracture detection because of the polarity changes that occur when crossing the principle axes. Furthermore, if birefringence is present and uncorrected, it degrades the image (e.g. Bale et al., 2000). Azimuthal anisotropy is also referred to as transversely isotropic with a horizontal symmetry axis, or "HTI".

Clearly this goal has some influence on the choice of algorithm. For an excellent comparative review of modern modelling techniques, see Carcione et al. (2002). For the sake of brevity, the following analysis considers only the most likely candidates.

One possibility, ray-tracing, can be adapted to elastic, anisotropic media (Červený et al., 1977), and has the advantage that aspects of the wavefield (e.g. specific modes) can

be isolated. The limitations of ray tracing are that it is based on high frequency asymptotic solutions to the wave equation, that it is not possible to simulate the full wavefield, and that it fails in the presence of caustics. Some approaches overcome this latter restriction, for example by the use of Gaussian beams (e.g. Červený et al., 1982; Hill, 1990). Another important consideration is the complexity of the ray-tracing algorithm required for the fully anisotropic case.

A more attractive option is one of the grid methods, such as finite difference or finite element. These have the advantage of honouring low frequency behaviour and modelling the full wavefield. They also provide the ability to generate snapshots or movies of the wavefield. Their main disadvantages are cost and the inability to isolate specific events. Much of the complexity associated with modern finite-difference methods, such as variable grids and domain decomposition, is related to their CPU and memory demands. These arise primarily due to the number of nodes per wavelength required to accurately model the wavefield.

The pseudospectral method (Kosloff and Baysal, 1982) is an alternative grid based modelling method similar to finite-difference, but with one key difference. Instead of using difference operators, Fourier transforms are used to apply the spatial derivatives. It can be viewed as a limiting case of higher order finite-difference, when the operator size equals the grid dimension. In seismic modelling, the main advantage is that many fewer grid points per wavelength are needed to attain any desired accuracy. According to Fornberg (1987) a fourth order finite-difference code needs 4 times as many grid points per wavelength as the pseudospectral approach, for each dimension. Hence, it is particularly attractive for modelling in 3D. It is primarily for this reason, and the relative ease of coding required, that the pseudospectral approach is adopted here. The pseudospectral method also shares the other advantages of finite-difference methods, such as movie generation.

Like other techniques, the pseudospectral method has its own peculiar difficulties, including numerical dispersion, model discretization effects, boundary effects and non-local operator artifacts. These must be addressed in order to achieve acceptable results. Historically, the pseudospectral method may also have been avoided for 3D modelling due to the global nature of Fourier operators, and the resulting need to transpose the data when the complete wavefield could not be stored in core memory (Holberg, 1996). Now, with the availability of (relatively) inexpensive random access memory, this drawback no longer exists. The complete elastic wavefield, for moderate sized grids (i.e. sufficient in size for the pseudospectral method), can be stored in core memory.

Previous work using finite-difference or pseudospectral methods to simulate shear-wave birefringence includes Ramos-Martinez et al. (2000) and Fang (1998). Ramos-Martinez et al. used finite-difference modelling to analyze splitting for a range of different anisotropic symmetries ranging from HTI to monoclinic, in a 2.5-D medium. Fang used the pseudospectral method with second order finite-difference time derivatives to model elastic waves in a 2D medium with azimuthal (HTI) anisotropy.

In the first section of this paper I review the basic theory of elastic modelling using the pseudospectral method, including a brief outline of computational considerations. In the second section I describe the numerical issues that need to be addressed, and how this is

currently being done. A companion paper (Bale, 2002) considers one of these issues, non-local operator artifacts, in more detail. In the last section I present some results of pseudospectral elastic modelling for both 2D and 3D examples.

BASIC THEORY

Elastic modelling

The modelling of wave propagation in elastic, possibly anisotropic, heterogeneous media is based upon the following equation of motion:

$$\rho \ddot{u}_j = \sigma_{jl,l} + f_j, \tag{1}$$

where ρ is density, u_j is the component of displacement in the jth direction, and f_j is the body force which in this case is taken to be the source term.

Above, and throughout this paper, I use the convention that ",l" denotes partial differentiation with respect to x_l, the lth spatial coordinate, and also the Einstein summation convention whereby twice-repeated indices indicate an implied summation. Suffices repeated more than twice imply that the summation convention is suspended. All suffices take the values 1,2 and 3, and to clarify I use x,y and z when appropriate. Also $\ddot{u}$ indicates the second time derivative of u.

The stress-strain relationship (generalized Hooke's law) between the stress σ_{jl}, and the strain e_{mn}, is given by:

$$\sigma_{jl} = c_{jlmn} e_{mn}, \tag{2}$$

where c_{jlmn} is the 4th rank stiffness tensor. In turn the strain tensor is given by:

$$e_{mn} = \frac{1}{2}\left(u_{m,n} + u_{n,m}\right). \tag{3}$$

Equation 3 shows that the strain tensor is symmetric. Simple physical arguments can be used to show the symmetry of the stress tensor. These symmetries taken together imply that the stiffness tensor is symmetric under interchanges of j with l, m with n, and jl with mn. The result is, that for the most general elastic medium, there are "only" 21 independent elastic coefficients rather than the 81 of an arbitrary 4th rank tensor. Also the following coordinate transformation rule is useful for creating arbitrary symmetries:

$$c'_{ijkl} = \left(\frac{\partial x'_i}{\partial x_m}\right)\left(\frac{\partial x'_j}{\partial x_n}\right)\left(\frac{\partial x'_k}{\partial x_p}\right)\left(\frac{\partial x'_l}{\partial x_q}\right)c_{mnpq} \tag{4}$$

An alternative representation of the stiffness uses the Voigt notation to replace the 4th rank tensor c_{jlmn} by a symmetric 6x6 matrix **C** as follows:

$$\mathbf{C} \equiv \begin{bmatrix} c_{1111} & c_{1122} & c_{1133} & c_{1123} & c_{1113} & c_{1112} \\ & c_{2222} & c_{2233} & c_{2223} & c_{2213} & c_{2212} \\ & & c_{3333} & c_{3323} & c_{3313} & c_{3312} \\ & & & c_{2323} & c_{2313} & c_{2312} \\ & & & & c_{1313} & c_{1312} \\ & & & & & c_{1212} \end{bmatrix}, \tag{5}$$

where the lower half of the matrix is implied by symmetry.

The pseudospectral technique

In pseudospectral modelling the spatial derivatives are evaluated using multiplications by $-ik_j$ after first transforming to the wavenumber domain using a Fourier transform of the function along the appropriate spatial dimension, x_j. For example, to evaluate the term $u_{m,n} \equiv \partial u_m / \partial x_n$ in equation (3), the following inverse Fourier transform is used (suspending the summation convention):

$$\frac{\partial u_m}{\partial x_l}(\mathbf{x}) = \frac{1}{2\pi} \int_{-\infty}^{\infty} (-ik_l) \widetilde{u}_m^{(l)} e^{-ik_l x_l} dk_l, \tag{6}$$

where the Fourier transform of u_m with respect to the spatial variable x_l is:

$$\widetilde{u}_m^{(l)} = \int_{-\infty}^{\infty} u_m e^{ik_l x_l} dx_l. \tag{7}$$

The Fourier transform is applied along the direction given by the superscript (l). Also $i = \sqrt{-1}$.

Hence, to evaluate the "divergence" of stress $\sigma_{jl,l} \equiv \nabla_l \sigma_{jl}$ required for (1), the following is used:

$$\nabla_l \sigma_{jl}(\mathbf{x}) = \sum_{l=1}^{3} \left\{ \frac{1}{2\pi} \int_{-\infty}^{\infty} (-ik_l) \widetilde{\sigma}_{jl}^{(l)} e^{-ik_l x_l} dk_l \right\}, \tag{8}$$

where the summation over l is implied on the left hand side, but is explicitly written on the right hand side, since the summation convention is violated.

Unlike the spatial derivatives in pseudospectral modelling, the temporal derivatives used to step the wavefield forward in time are typically evaluated using a finite-difference approximation of some kind. This results in a disparity between accuracy of the spatial and temporal operators, and can give rise to numerical dispersion. I will address this issue in the "Numerical Issues" section.

Computational cost

The most significant contribution to cost of the pseudospectral method is performing Fourier transforms using the FFT (for the isotropic case, the cost of calculating the stress using equation (2) is also almost negligible, though this is not so for the anisotropic case). Hence, a useful guide to efficiency of the algorithm is a count of the number of Fourier transforms required.

Evaluating $\sigma_{jl,l}$ in equation (1) consists of:

1. Performing a Fourier transform along each spatial direction for each component (a total of $3M$ FFTs where $M=N_x.N_y+N_x.N_z+N_y.N_z$ and N_ξ is the number of grid points in the ξ direction).

2. Applying equation (6) for each component and each spatial direction, and combining them using (3) to get e_{mn} (this entails $3M$ inverse FFTs)

3. Multiplying by the stiffness tensor using (2), to get σ_{jl}

4. Performing a Fourier transform along each spatial direction, l, for σ_{jl} (another $3M$ FFTs)

5. Using equation (8) to evaluate the second spatial derivative with respect to x_l (another $3M$ FFTs).

Note that the total is $12M$ FFTs ($6M$ forward and $6M$ inverse).

In the case when the medium is homogeneous, the stiffness tensor may be exchanged with the second derivative to give the homogeneous wave equation:

$$\rho\ddot{u}_j = c_{jlmn}u_{m,nl} + f_j \tag{9}$$

This assumption gives an apparent computational advantage, since there is no need to do any Fourier transforms between the first and second derivatives.

This approach might be thought useful (and appears to be suggested by some authors: e.g. Lou and Rial, 1995) in the case where the medium is slowly varying, such that derivatives $c_{jlmn,l} \equiv \partial c_{jlmn}/\partial x_l$ of the stiffness tensor can be neglected.

However, to exploit this advantage, it is necessary to apply (9) in the Fourier domain, to reduce the rank of the tensor from 3 to 1 before applying the inverse Fourier transform. This is only legitimate for a totally invariant medium. Even for a slowly varying medium (9) must be performed in the spatial domain. Hence it would be necessary to first evaluate $u_{m,nl}$ by inverse Fourier transforms. Evaluation of $u_{m,nl}$ entails a total of $27M$ inverse Fourier transforms, since every one of the 9 combinations arising from multiplication by $(-k_n\,k_l)$ for $n=1,...,3$ and $l=1,...,3$ must be separately computed, for $m=1,...,3$. For this reason, the more accurate heterogeneous approach, using equations (1) and (2), is also the more efficient method, except for the (usually uninteresting) case of a homogeneous medium.

NUMERICAL ISSUES

Wraparound and absorbing boundaries

Finite-difference methods are susceptible to artificial reflections from the boundaries unless appropriate counter measures are taken. A common approach to dealing with this problem is to adopt a one-way wave equation at the borders, so that waves pass outwards only. This completely suppresses the reflections in the 1D case, but is less than perfect for higher dimension grids.

The pseudospectral method is based on periodic Fourier basis functions, so the corresponding problem is not artificial reflection, but grid wrap-around. Waves exiting from the bottom of the grid reappear at the top and vice versa. Similarly waves exiting the right side of the grid will reappear at the left and vice versa. Obviously the one-way wave equation approach is of no use here, since the waves would still wrap around to the opposite side.

Instead, I use a simple but reasonably effective approach, devised by Cerjan et al. (1985). The wavefield and its time derivative are multiplied by a gentle taper function $\exp(-\alpha(x - \bar{x})^2)$ within a border zone near the grid boundary, after each time-step. The result is that waves propagating into the borders are suppressed gradually to very low amplitudes as they reach the edge. This works well for normally incident waves but suffers from reflections of low-wavenumber energy at oblique angles. A more recent method, known as the perfectly matched layer (PML), was originally developed for electromagnetic problems by Bérenger (1994), and has been successfully used for elastic wave problems (Collino and Tsogka, 2001). PML solves the oblique incidence problem by applying absorption only to the component of the wavefield normal to the boundary. Adopting PML is an obvious possible improvement to the current modelling code.

Dispersion and higher order time marching

Consider the following second order central difference approximation to the second derivative:

$$\ddot{u}_j(t) \equiv \frac{\partial^2 u_j}{\partial t^2}(t) \cong \frac{u_j(t + \Delta t) - 2u_j(t) + u_j(t - \Delta t)}{(\Delta t)^2} \qquad (10)$$

where the time discretization step Δt, is also the sample interval of the wavelet and modeled output. Application of (10), combined with Fourier domain spatial derivatives, results in numerical dispersion (frequency dependent velocity), which can be analytically computed, as discussed in Appendix A. As shown in Figure 1, the dispersion can be reduced by choosing small time-steps (incurring additional computational cost), but not eliminated.
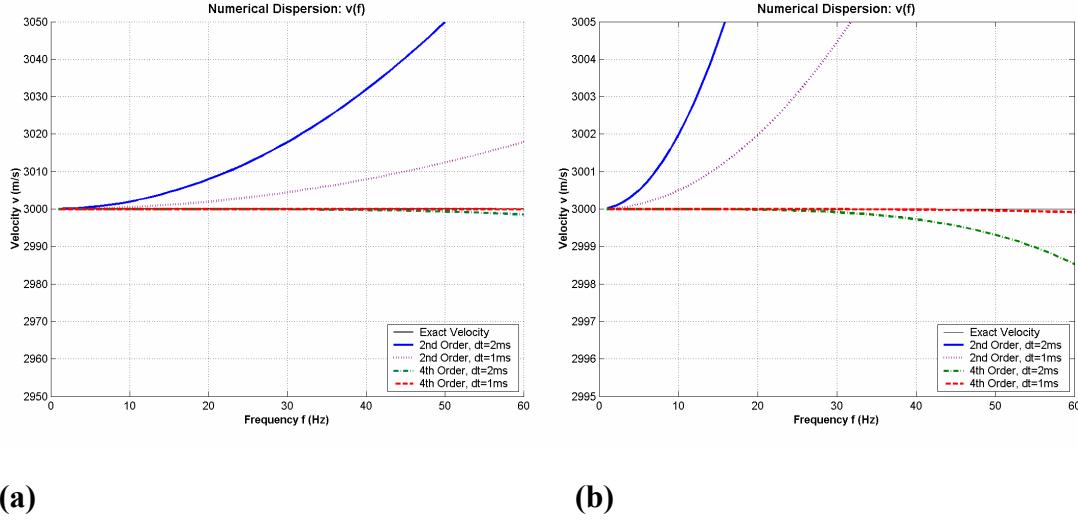
(a)   **(b)**

FIG. 1: Numerical dispersion, for 2nd and 4th order difference approximations, as a function of frequency from 0-60Hz, with c = 3000m/s. The graphs in (a) and (b) show the same curves, but with velocity ranges of 100 m/s and 10 m/s respectively. Phase velocity for the 2nd order correction, computed using equation (A5), is plotted for Δt = 2ms (solid blue line) and Δt = 1ms (dotted purple line). Phase velocity for the 4th order correction, computed using equation (A6), is plotted for Δt = 2ms (dot-dash green line) and Δt = 1ms (dashed red line). The solid black line shows the exact velocity of 3000m/s. From (b) it is seen that the 4th order correction with 1ms sampling is almost exact.

The form of the dispersion can be determined and corrected for any specific velocity, as described in the appendix, but not for multiple velocities or mode types. Instead, an alternative approach to reducing dispersion is the use of higher order derivatives. I follow the approach described in Dablain (1986), starting from Taylor series expansions of $u_j(t - \Delta t)$ and $u_j(t + \Delta t)$:

$$u_j(t \pm \Delta t) = u_j(t) \pm \Delta t \frac{\partial u_j(t)}{\partial t} + \frac{(\Delta t)^2}{2} \frac{\partial^2 u_j(t)}{\partial t^2} \pm \frac{(\Delta t)^3}{3!} \frac{\partial^3 u_j(t)}{\partial t^3} + \frac{(\Delta t)^4}{4!} \frac{\partial^4 u_j(t)}{\partial t^4} + O\left((\Delta t)^5\right)$$

(11)

Substituting into the right hand side of equation (10) cancels all the odd derivatives, and gives the difference approximation:

$$\frac{u_j(t + \Delta t) - 2u_j(t) + u_j(t - \Delta t)}{(\Delta t)^2} = 2\left[\frac{1}{2} \frac{\partial^2 u_j(t)}{\partial t^2} + \frac{(\Delta t)^2}{4!} \frac{\partial^4 u_j(t)}{\partial t^4} \right] + O\left((\Delta t)^4\right) \quad (12)$$

If only the first term on the right side is retained we get the standard 2nd order approximation, but keeping both terms gives 4th order accuracy (this could, of course, be extended with more terms to arbitrary accuracy). Both terms on the right hand side must be replaced by spatial derivatives. The first term comes directly from equation (1). The key step, known as the Lax-Wendroff correction (Lax and Wendroff, 1964), is to replace the second term in equation (12) by spatial derivatives.

Making use of the relationship in equations (1), (2) and (3):

$$\rho \frac{\partial^4 u_j(t)}{\partial t^4} = \rho \frac{\partial^2}{\partial t^2}\left(\frac{\partial^2 u_j(t)}{\partial t^2}\right)$$

$$= \frac{\partial^2}{\partial t^2}\left(\sigma_{jl,l} + f_j(t)\right)$$

$$= \left(\frac{\partial^2 \sigma_{jl}(t)}{\partial t^2}\right)_{,l} + \frac{\partial^2 f_j(t)}{\partial t^2} \tag{13}$$

$$= c_{jlmn}\ddot{u}_{m,nl} + \ddot{f}_j$$

which amounts to applying the linear operator in (1) but using $\ddot{u}$ (itself computed from (1)) and $\ddot{f}$ (computed analytically, or by using Fourier transforms) in place of u and f.

The dispersion associated with use of the 4th order correction in equation (12) is considerably less than that of the 2nd order equation (10), as can be seen in Figure 1.

After dropping $O\left((\Delta t)^4\right)$ terms, equation (12) can be separated (following Lou and Rial, 1995) into the following equations, which are used for the time marching steps:

$$\frac{\partial u_j}{\partial t}\left(t + \Delta t/2\right) \cong \frac{\partial u_j}{\partial t}\left(t - \Delta t/2\right) + \Delta t\left(\frac{\partial^2 u_j}{\partial t^2}(t) + \frac{(\Delta t)^2}{12}\frac{\partial^4 u_j}{\partial t^4}(t)\right)$$

$$u_j\left(t + \Delta t\right) = u_j(t) + \Delta t\frac{\partial u_j}{\partial t}\left(t + \Delta t/2\right) \tag{14}$$

For each time-step the modelling proceeds by computing $\ddot{u}_j \equiv \partial^2 u_j/\partial t^2$ and $\partial^4 u_j/\partial t^4$ using equations (1) and (13), and then using equation (14) to step forward both $\dot{u}_j$ (i.e. velocity) and u_j. For the duration of the source wavelet, the force term f_i in equation (1) is equal to the successive samples of the wavelet at the grid position of the source. Subsequently there is no force term. Likewise $\ddot{f}$, in equation (13), is injected sample by sample for its duration.

Staggered grids and anisotropy

The modelling is performed using staggered grids to make the Fourier odd derivative operators compact (Özdenvar and McMechan, 1996; Carcione, 1999; Corrêa et al., 2002). The staggering works exactly for isotropic media or anisotropic media that is aligned with the grid (at least orthorhombic symmetry). For non-aligned anisotropy, such as HTI with principle axes at some angle other than 0° or 90° to the grid, the staggering is exact for only part of the stiffness tensor. The details of this technique are given in a companion paper (Bale, 2002).

Non-aligned interfaces and anisotropy

The main advantage of the pseudospectral method may also be its Achilles heel. The use of the Fourier domain for applying derivatives allows accurate modelling with as few as two grid points per wavelength. This means that the medium parameters are also discretised relatively coarsely, compared to, say, finite-difference. This is perfectly acceptable for interfaces (model changes) that are aligned with the grid, but results in a "staircase" type interface when they are not. The consequence is the presence of spurious diffractions in the data, originating from the corners of the steps in the staircase. Various solutions to this problem have been proposed, but the one which seems to best accommodate anisotropy is that given by Muir et al. (1992). Their approach is to regard each grid point as the center of a cell. In the case of interfaces crossing a cell they use Schoenberg-Muir calculus (Schoenberg and Muir, 1989) to average properties for the cell after an appropriate tensor rotation. I have implemented this technique for the 2D case, and found it reasonably successful at suppressing the unwanted diffractions. However, the examples in this paper are all grid aligned.

RESULTS

The pseudospectral code was written using MATLAB 6.5. The modelling examples all ran on a desktop machine equipped with a 2.27GHz Pentium 4 CPU and 512MB of RAM, except for the 2D example which ran on a laptop with a 775 MHz Pentium 3 CPU. For the 3D elastic examples running on the Pentium 4 the memory available effectively limited the maximum model size to about 1 million grid nodes, or 128x128x64 nodes. Although this is usually considered a rather small grid for numerical modelling, the pseudospectral limit of two grid nodes per wavelength allows reasonable sized physical dimensions of the modelling domain.

Comparison with 3D analytic solution

To test the algorithm for a simple homogeneous isotropic example, I compare with the analytic solution given by Aki and Richards (1980) for a point dislocation source (see Appendix B). The calculation uses a 64x64x64 grid with 20 meter spacing, and a time-step of 2 ms. The source, located at the center of the grid, has a Ricker wavelet time signature with center frequency of 20hz. The Ricker wavelet and its second derivative, used for equation (13), are shown in Figure 2. Receivers are located at the positions listed in Table 1, lying along a vertical slice that is diagonal in x and y. The receiver positions are such that the wavefield is sampled along one vertical and one horizontal axis, and also along 2 diagonal directions.

The results for the X and Z component responses are shown in Figure 3. With the exception of some small differences for the P-wave arrival on receiver 2, directly below the source, the pseudospectral and analytical results are indistinguishable.

Table 1: Receiver positions relative to source at grid center.

Receiver Number	1	2	3	4
x (m)	200	0	200	-200
y (m)	200	0	200	-200
z (m)	200	200	0	200

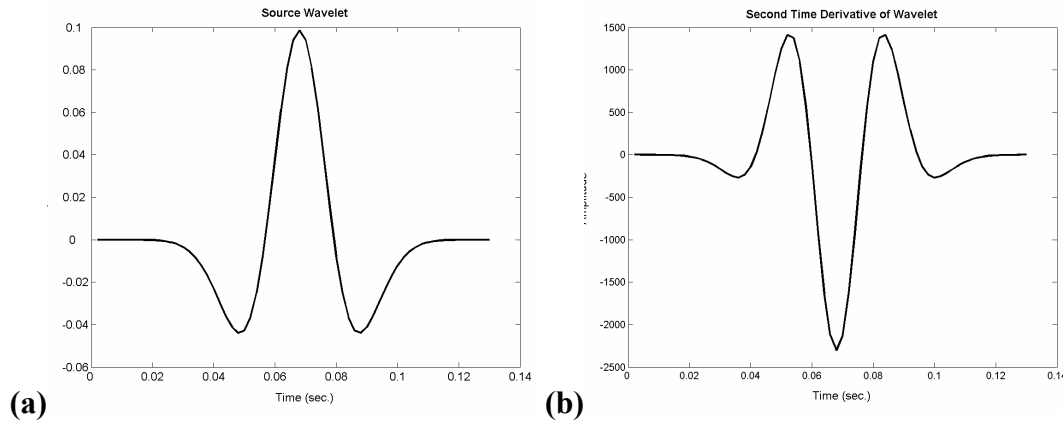**(a)**   **(b)**

FIG. 2: The source signature, a 20 Hz Ricker wavelet (a), and its second time derivative (b).

2D layered medium

A 2D version of the modelling code was applied to the layered model shown in Figure 4. The modelling is done first with isotropic velocities in all layers, and then with azimuthally anisotropic (HTI) velocities in the second layer. For the anisotropic case, the stiffness matrix is based on the parameters of Lou and Rial (1995; Table 3). They used Hudson theory with a crack density, *CD*=0.1 (where $CD \equiv Na^3/V$ for *N* cracks of radius *a*, an a volume *V*). I have scaled their values by 0.31 to get slower velocities. The resulting stiffness matrix is given below in Table 2 (symmetry axis coordinate system) and Table 3 (grid coordinate system). The phase velocities are shown in Figure 4(d).

Table 2: c_{ijkl} for HTI model with symmetry axis in x direction. Values, in GPa, are obtained by scaling Lou and Rial (1995) Table 3 by 2/3.

ij \ kl	11	22	33	23	13	12
11	11.1	3.275	3.275	0	0	0
22	3.275	11.65	4.25	0	0	0
33	3.275	4.25	11.65	0	0	0
23	0	0	0	3.7	0	0
13	0	0	0	0	2.85	0
12	0	0	0	0	0	2.85

Table 3: c_{ijkl} for HTI model with symmetry axis at 45° to x direction, by rotation of c_{ijkl} in Table 2.

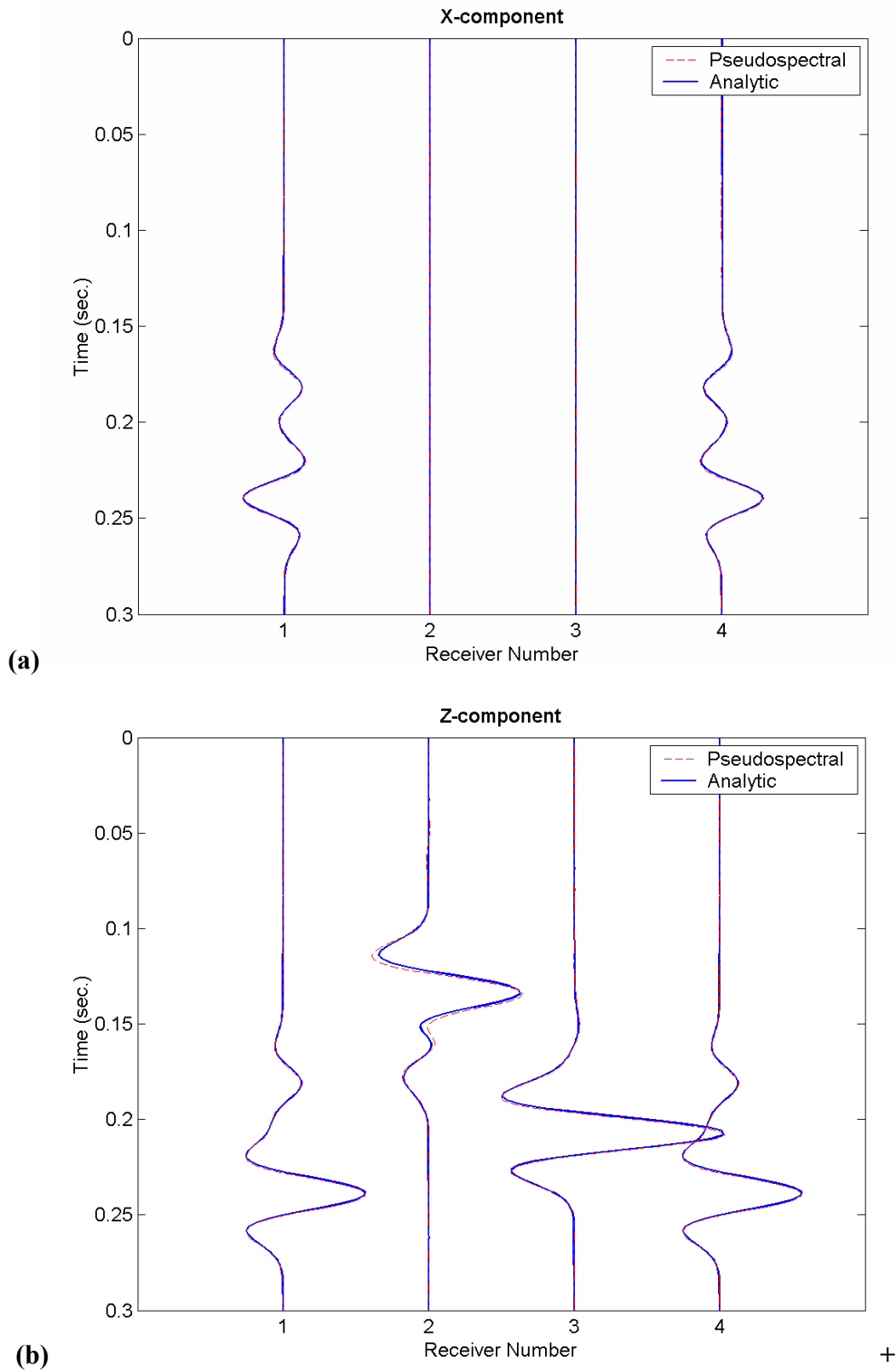| ij \ kl	11	22	33	23	13	12
11	10.175	4.475	3.7625	0	0	0.1375
22	4.475	10.175	3.7625	0	0	0.1375
33	3.7625	3.7625	11.65	0	0	0.4875
23	0	0	0	3.275	0.425	0
13	0	0	0	0.425	3.275	0
12	0.1375	0.1375	0.4875	0	0	4.05

FIG. 3: Time history comparison between the pseudospectral result (red dashed) and analytic result (blue solid) for horizontal in-line component (a), and for vertical component (b), for isotropic homogeneous model. Receiver numbers correspond to positions listed in Table 1.
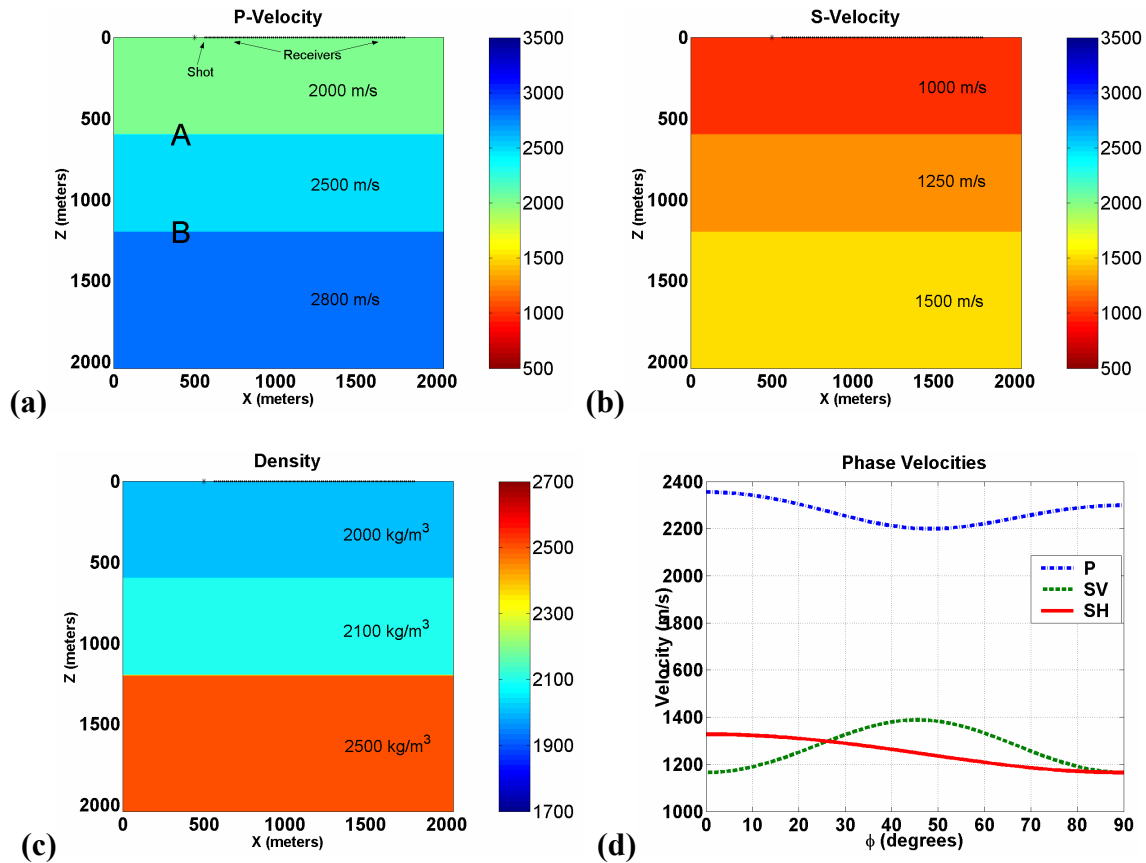
FIG. 4: Layered model for 2D example. The P- and S-wave velocities for the isotropic model are shown in (a) and (b). The density is shown in (c). For the anisotropic example the middle layer is replaced by the HTI layer defined in Table 2. The phase velocities for this layer, measured as a function of azimuth, ϕ, from the symmetry axis direction, are shown in (d).

The source is a vertical displacement point force with a 15Hz Ricker signature. It was placed at 500m from the left hand edge of the model. One hundred 3-C (X-Y-Z) receivers were placed at 12.5m intervals between 562.5m and 1800m from the left hand edge. Both source and receivers were on the top edge of the model, with a free surface boundary condition. The grid size was 256x256; the grid spacing is 8m along both directions. The wavefield was modeled using 2000 time-steps of 1ms each.

Figure 5(a) shows the shot record generated by isotropic modelling. Both pure reflections (P-P, S-S) and converted wave reflections (P-S, S-P) are easily identified on the in-line (X-component) and vertical (Z-component) receivers. The conversions during transmission are much weaker, and are not annotated. The cross-line (Y-component) receiver doesn't record any response, since no SH-wave is generated in this case. Figure 5(b) shows the shot record generated by modelling in the HTI model. The presence of azimuthal anisotropy in the second layer gives rise to some new features. First, the Y-component responds to reflections arising from both top and bottom of that layer. The response from the top is interesting as it demonstrates (as expected) an anisotropic reflection coefficient. Second, the wave-modes that are transmitted through this layer (in particular, the later P-S event) are clearly split into two distinct arrivals. This is the evidence of shear-wave splitting.
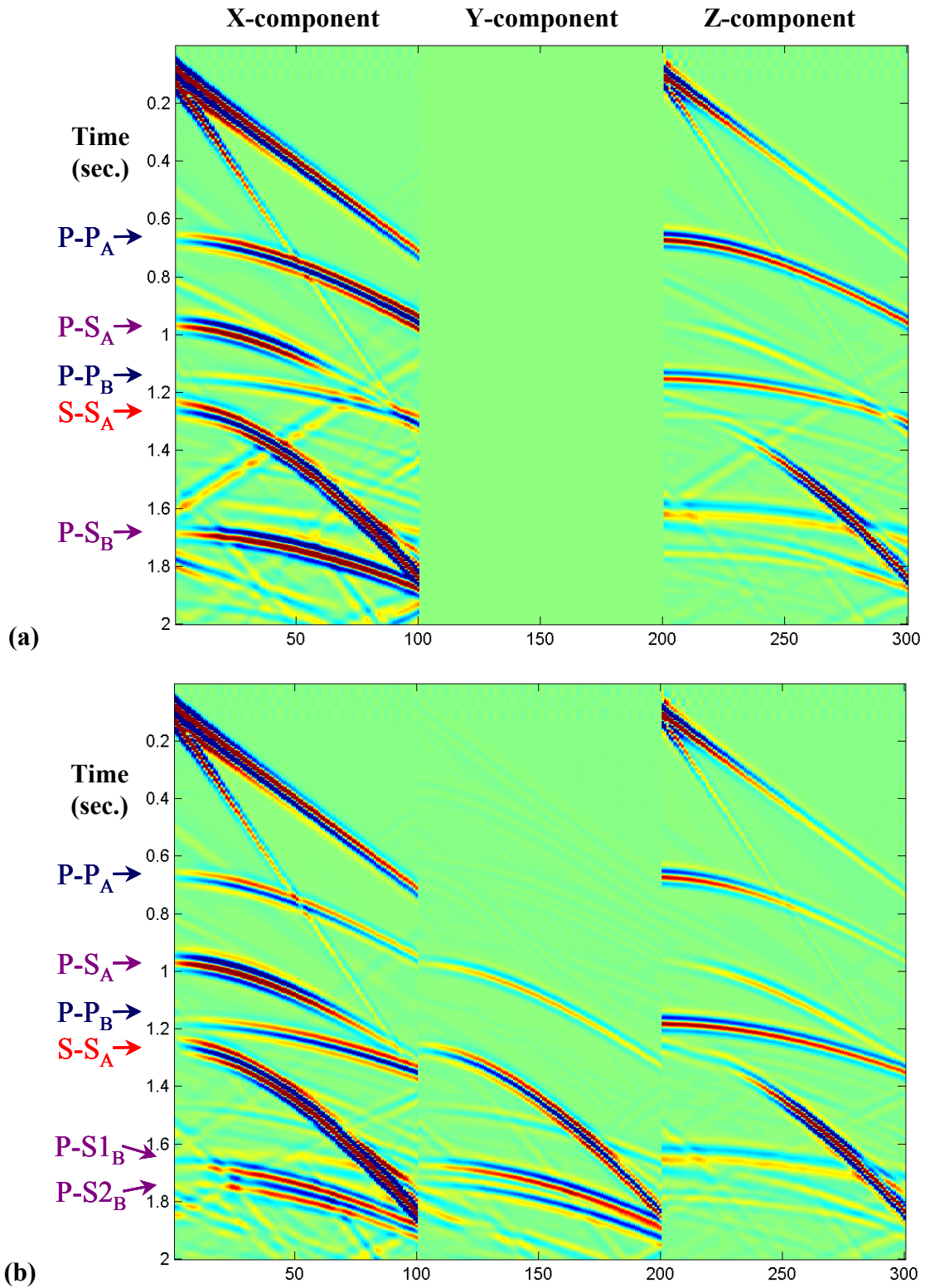
FIG. 4: Isotropic vs. HTI modelling in 3 layer medium. Figures show X, Y and Z component responses to vertical displacement source over three layered medium where second layer is: (a) isotropic and; (b) HTI with a symmetry axis at 45° to the in-line direction. Events annotated for pure and converted reflections from interfaces A and B in Figure 3(a). Note the presence of split shear-waves on the PS conversion from interface B in (b).

3D homogeneous isotropic vs. HTI

The 3D examples are simple in concept, but give rise to complex wavefields that require some careful analysis. The medium is homogeneous, with two different scenarios: one in which it is also isotropic and a second in which it is azimuthally anisotropic, having HTI with a symmetry axis at 45° to the in-line (x) direction. For the isotropic case, the parameters are as follows: V_P=3000 m/s, V_S=2000 m/s and ρ=2000kg/m^3. For the anisotropic case, the stiffness matrix is given by Table 4.

Modelling is done on a grid with nx=ny=128 and nz=64. The grid spacing is 20m along all 3 axes. The source, a vertical displacement with a 20Hz Ricker spectrum, is located at the center of the grid. Receivers are set in a "common offset ring" of radius 300m at a depth of 160 meter below the surface, in order to eliminate boundary effects. An absorbing boundary is used on all sides, of width 16 points for the vertical sides, and 8 points (160 meters) for the top and bottom. The model geometry is shown in Figure 5.

The source generates both P- and S-waves which are recorded at the receiver locations. Snapshots of the wavefield are shown in Figures 6 and 7, for the isotropic and HTI cases respectively. In the isotropic case (Figure 6) both P- and S-wave polarizations are confined to the plane of propagation. So, for example, an x-z slice (i.e. constant y coordinate) taken through the source position, shows only a response on the X and Z components (Figure 6a).

In the HTI case however, this is no longer true. The P-wave polarization does remain in the propagation plane, but the S-wave excites particle motion out of the propagation plane, due to the anisotropic response. The onset of shear-wave splitting is also visible, although the two S-wave surfaces are not sufficiently separated to avoid interference with one another.

Figure 8 shows the seismic records at the receiver common offset ring. The isotropic results (a)-(c) are readily understood. The amplitude varies sinusoidally on both horizontal components, as the radial direction varies between in-line (x), cross-line (y), anti-in-line and anti-cross-line. For instance, as the azimuth passes through a direction 90° from in-line, the expected polarity change occurs on the X component (Figure 8a).

The HTI results in Figure 8 (d)-(f) are less intuitive. There is clear variation in arrival time with azimuth for both P- and S-wave arrivals. In the S-wave case, this variation is associated with the developing of a fast and slow shear-wave, due to splitting. On the horizontal components, the P-wave arrival maintains the polarity behaviour seen in the isotropic case, whereas the S-wave arrival displays a shift in the position of the polarity change relative to the isotropic case. In the case of totally split shear-waves it would be expected that these nulls occur at an azimuth orthogonal to the principle axis for that mode. In other words, we would expect the slow shear-wave to vanish along the fast direction and vice versa. In the case modeled here the splitting is incomplete, and so the nulls occur in intermediate locations.

The behaviour observed here is representative of what one may expect for a converted wave experiment with a complete coverage of azimuths at some non-zero offset. Here, the displacement source at depth plays the role of the mode conversion. An obvious question, and one of importance for converted-wave exploration is whether one could

infer the direction of the principle axes from the data in Figure 8. A detailed study of this question is beyond the scope of this paper, but an initial evaluation has been done.

Figure 9 shows graphs of particle motion or "hodograms" in the XY plane for both the isotropic (a) and HTI (b) model data. These hodograms use time windows which cover the shear-wave arrival. They give an indication of the observed polarization., both its direction and its degree of linearity. The isotropic hodograms are consistent with purely radial polarizations, as expected. The HTI hodograms in this case show non-linearity for all azimuths other than those of the principle axes of anisotropy. However, the degree of non-linearity is relatively small except for azimuths around 105°, 165° and their 180° opposite angles. This raises doubt whether, in this case, a robust estimation would be possible in the presence of noise, based on hodograms. It remains to be seen whether other methods such as Alford rotation (Alford, 1986) or 3D variants on that theme (Gaiser, 2000) would succeed here.

Table 4: c_{ijkl} for HTI model with symmetry axis at 45° to x direction, all values in GPa.

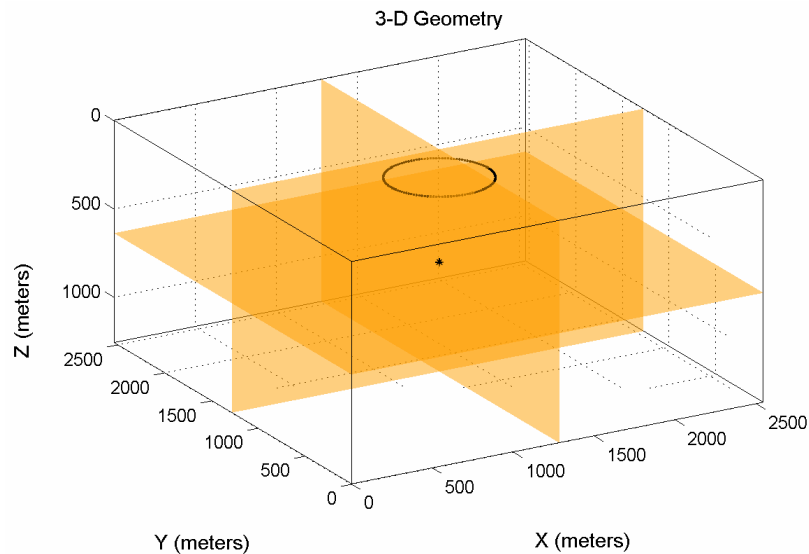| ij \ kl	11	22	33	23	13	12
11	21.7	9.52	8.045	0	0	0.315
22	9.52	21.7	8.045	0	0	0.315
33	8.045	8.045	24.86	0	0	1.055
23	0	0	0	6.985	0.895	0
13	0	0	0	0.895	6.985	0
12	0.315	0.315	1.055	0	0	8.62

FIG. 5: Geometry of the 3D model example. The source is at the center of grid, position x=1280m, y=1280m, z=640m, indicated by the * in the figure. There are 120 receivers located at a depth of 160m, in a circle centered on the grid, with 3° azimuthal sampling. The horizontal source-receiver offset is 300m. Also shown are three perpendicular planes through the source with constant x, y and z respectively. These planes are used to show slices of the wavefield in Figures 6 and 7.
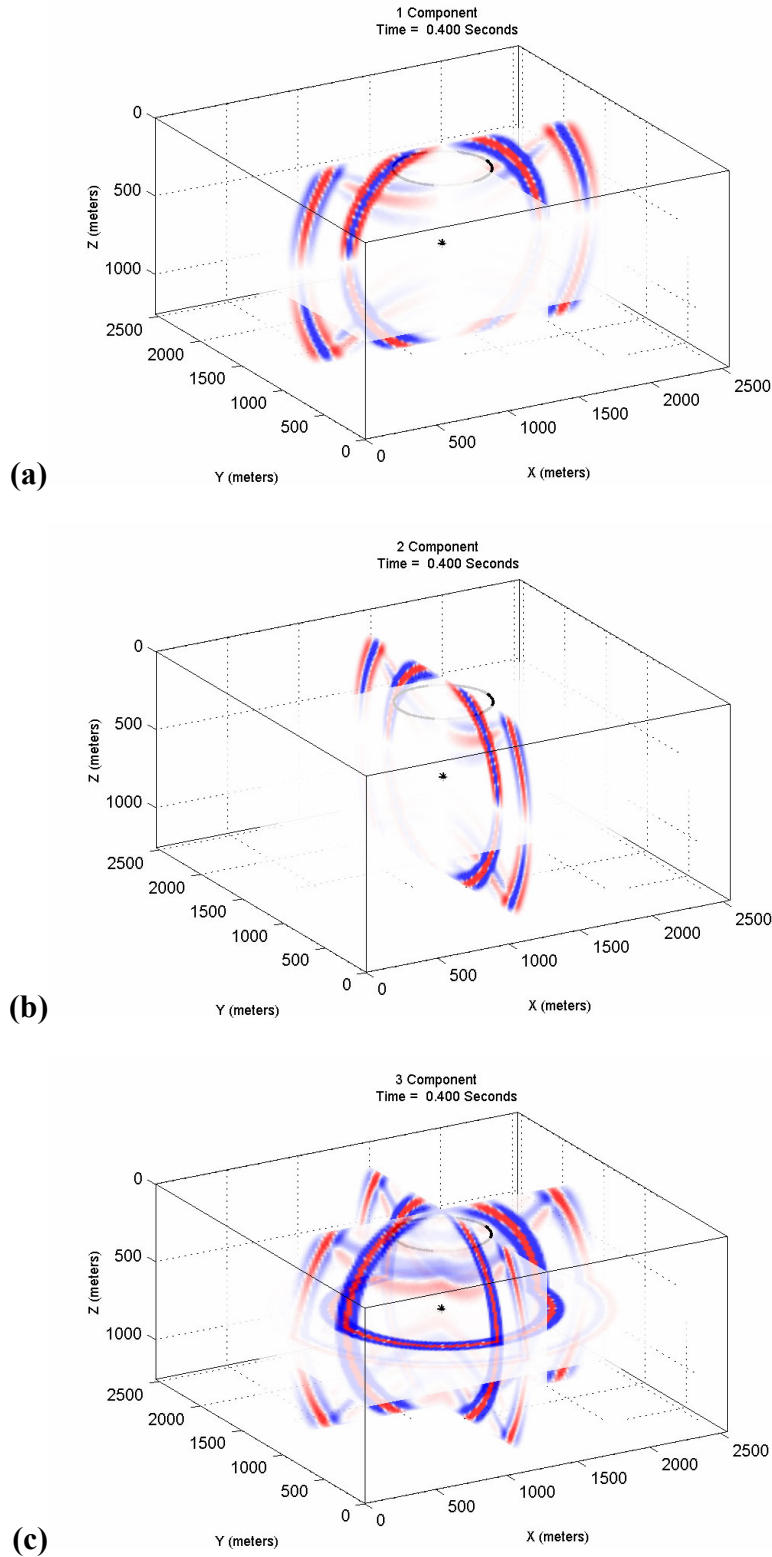
FIG. 6: Snapshots of X-component (a), Y-component (b) and Z-component (c) displacements, after 0.4 seconds, from modelling in homogeneous isotropic medium. Shear-wave polarizations are confined to propagation planes. The locations of the source in the center, and of the receiver ring near the surface are shown in black.
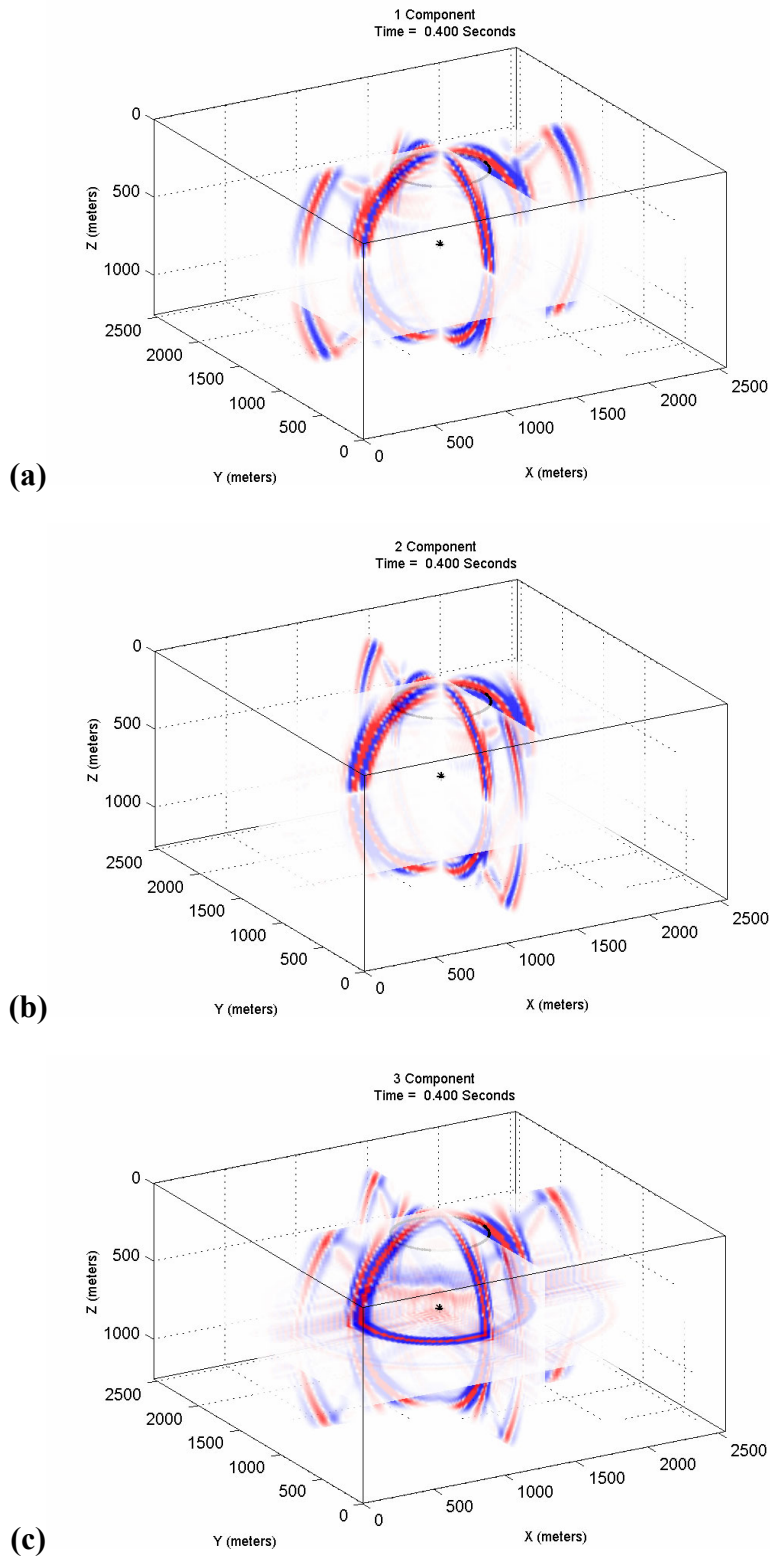
(a)

(b)

(c)

FIG. 7: Snapshots of X-component (a), Y-component (b) and Z-component (c) displacements, after 0.4 seconds, from modelling in homogeneous HTI medium, with 45° rotation of symmetry axis relative to in-line (x) direction. Shear-waves exhibit horizontal polarization, which is no longer confined to propagation plane (see constant x and constant y planes), due to splitting.
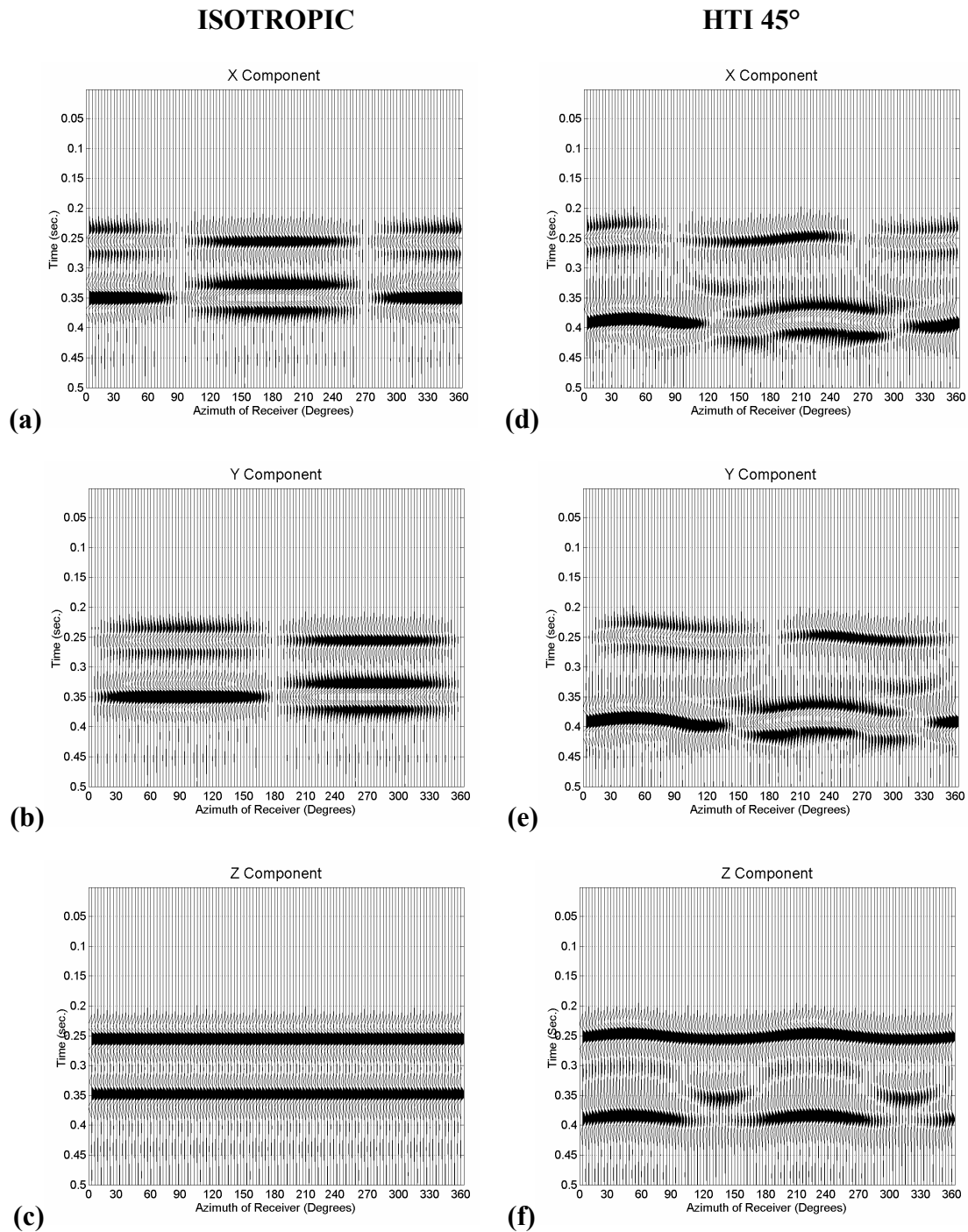
ISOTROPIC   **HTI 45°**

(a)   **(d)**

(b)   **(e)**

(c)   **(f)**

FIG. 8: Seismic records for X, Y and Z component receivers in "common offset ring" shown in Figure 5. The isotropic case, corresponding to Figure 6, is shown in (a-c). The HTI case, corresponding to Figure 7, is shown in (d-f).
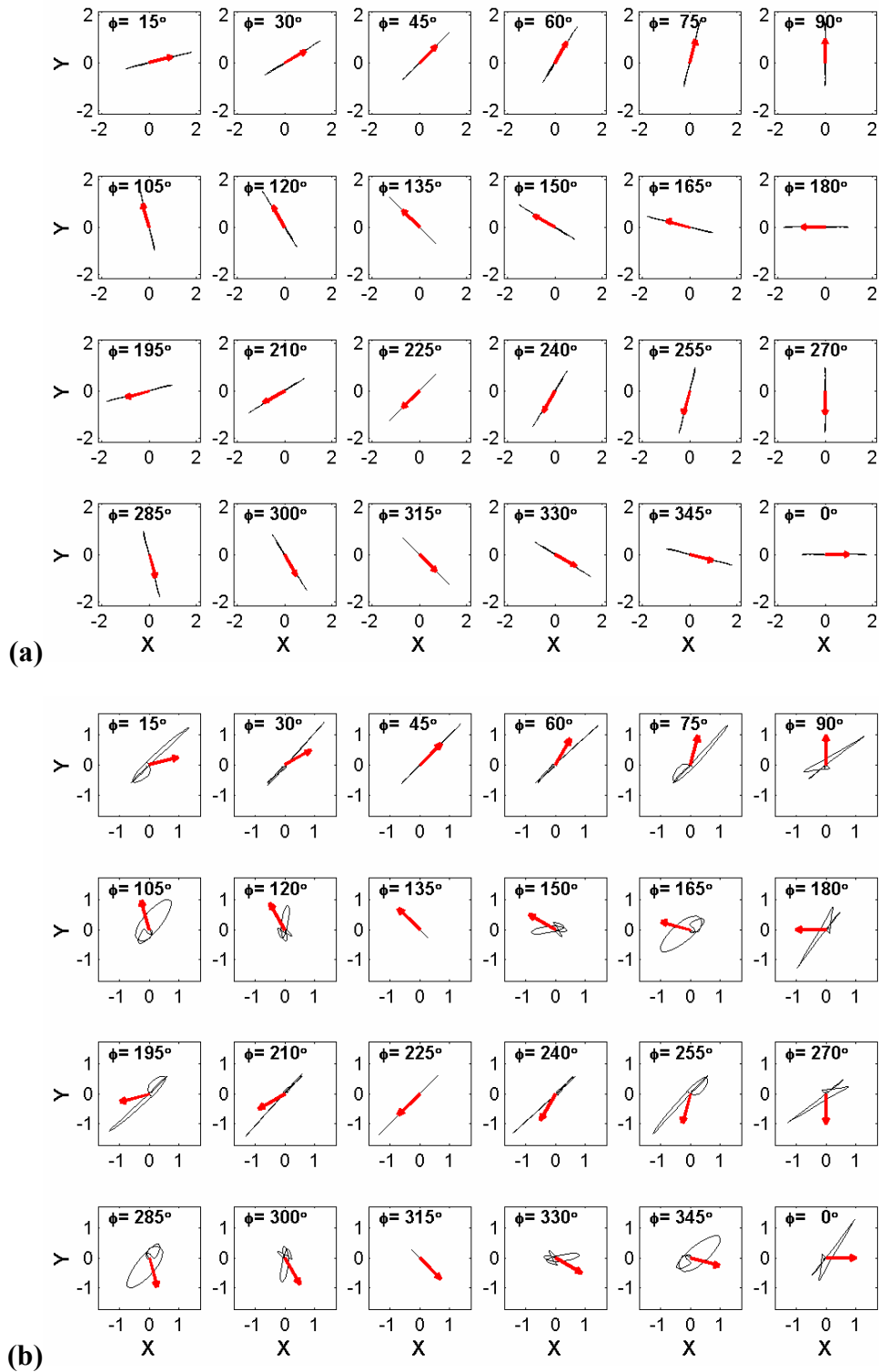
(a)

(b)

FIG. 9: Horizontal component hodograms for receivers at 15° increments for isotropic model (a), and 45° HTI model (b). Hodograms are computed over window from 0.3-0.45 seconds, corresponding to shear-wave arrival (see Figure 8). The red arrows indicate the source-receiver radial direction, which the particle motion is expected to follow in the isotropic case. For the HTI case, the hodograms align with the radial direction at the principle axes (45°, 135°, 225° and 315°), but otherwise are non-linear, due to fast and slow S-wave interference.

Runtimes

The runtimes for pseudospectral modelling are strictly linear in the number of time-steps taken. The relationship between runtimes and the number of grid-nodes can be expected to be slightly greater than linear, due to the FFT being proportional to *Nlog(N)*. The small 3D test used to validate the algorithm took about 20 minutes for 200 time-steps on a 64x64x64 grid, running on a 2.27GHz Pentium 4 with 512Mb RAM.

For 250 time-steps on a 128x128x64 grid, using the same hardware, the isotropic 3D modelling took approximately 2.5 hours, equivalent to 2 hours for 200 steps. Hence an increase by a factor of 4 in the model size gives an increase in runtime of 6. This is in part due to the *log(N)* term in the FFT cost, and in part caused by a small increase in paging to disk for the larger model. By comparison, the anisotropic 3D modelling took 5.5 hours CPU for the larger model.

I found that increasing the grid size to 128 in all directions (on the same machine) increased runtimes by an order of magnitude, due to excessive paging to disk. However, it should be expected that by increasing the RAM available to 1Gb, isotropic modelling on a grid of 128x128x128 could be done within 5 hours for 200 steps, and anisotropic modelling in approximately 12 hours. So 1000 time-steps, giving 2 seconds of data at 2ms sampling, would take under 3 days.

CONCLUSIONS

The pseudospectral method provides an accurate, efficient means to perform 3D elastic modelling in anisotropic heterogeneous media. Its *accuracy* results from using exact spatial derivatives applied in the Fourier domain. This is combined with fourth order time-marching to reduce dispersion. A comparison against an analytic solution was used to verify accurate modelling. The use of a staggered grid is also necessary to avoid generation of non-local operator artifacts associated with model interfaces. Its *efficiency* results from requiring only 2 grid points per minimum wavelength.

Elastic modelling in azimuthally anisotropic media using shows behaviour such as shear-wave splitting, whereby differently polarized shear-waves propagate with differing speeds. This was observed both for 2D and 3D examples. An analogue to converted-wave acquisition consists of a vertical displacement source at depth, and receivers near the surface. When these receivers are radially arranged around the source the polarization observed is non-linear except for azimuths parallel or perpendicular to the symmetry axis.

The cost of modelling fully 3D anisotropic elastic data is expensive but not prohibitive, and does not necessarily require specialized hardware. Obviously, however, modelling anything more than a small number of shot records would necessitate either the use of parallel hardware such PC clusters, or a very great deal of patience.

FUTURE WORK

With regard to the modelling algorithm itself, an anticipated improvement is to adopt PML absorbing boundaries (Bérenger, 1994; Collino and Tsogka, 2001). A possible

extension is to incorporate viscoelasticity, following work done by Carcione et al.(1988) and Carcione (1995, 1999).

However, as indicated in the introduction, development of the modelling code is a means to an ends. The focus for future work will be on generating 2D and 3D multicomponent synthetic datasets with shear-wave splitting in heterogeneous media, such as: dipping layers over HTI media; tilted fractures (TTI media). That notwithstanding, the code is general and could equally be used for other modelling enterprises such as modelling propagation through gas clouds.

ACKNOWLEDGEMENTS

REFERENCES

Aki, K. and Richards, P.G., 1980, Quantitative Seismology: Theory and Methods, Vol.1: New York, W.H.Freeman and Co.

Alford, R. M., 1986, Shear data in the presence of azimuthal anisotropy: Dilley, Texas: 56th Ann. Internat. Mtg., Soc. Expl. Geophys., expanded Abstracts, 476–479

Bale, R. A., 2002, Staggered grids for 3D pseudospectral modelling in anisotropic elastic media: CREWES Research Report, Vol. **14** (this volume).

Bale, R., Dumitru, G, and Probert, T., 2000, Analysis and stacking of 3D converted-wave data in the presence of azimuthal anisotropy: 70th Annual Internat. Mtg. Soc. Expl. Geoph., Expanded Abstracts, 1189-1192.

Bérenger, J. P., 1994, A perfectly matched layer for the absorption of electromagnetic waves: J. Comput. Phys., **114**, 185–200.

Carcione, J. M., 1995, Constitutive model and wave equations for linear, viscoelastic, anisotropic media: Geophysics, **60**, 537-548.

Carcione, J. M., 1999, Staggered mesh for the anisotropic and viscoelastic wave equation: Geophysics, **64**, 1863-1866.

Carcione, J. M., Herman, G. C. and ten Kroode, A. P. E., 2002, Seismic modelling: Geophysics **67**, 1304-1325.

Carcione, J. M., Kosloff, D., and Kosloff, R., 1988, Wave-propagation simulation in a linear viscoelastic medium: Geophys. J. Roy. Astr. Soc., **95**, 597-611.

Cerjan, C., Kosloff, D., Kosloff, R. and Reshef, M., 1985, A nonreflecting boundary condition for discrete acoustic and elastic wave equations: Geophysics, **50**, 705-708.

Červený, V., Molotkov, I.A., and Pšenčík, I., 1977, Ray Method in Seismology, Univerzita Karlova, Praha.

Červený, V., Popov. M. M. and Pšenčík, I., 1982. Computation of wave fields in inhomogeneous media - Gaussian beam approach: Geophys. J. Roy. Soc, **70**, 109-128.

Collino, F. and Tsogka, C., 2001, Application of the perfectly matched absorbing layer model to the linear elastodynamic problem in anisotropic heterogeneous media: Geophysics, **66**, 294-307.

Corrêa, G. J. P., Spiegelman, M., Carbotte, S., and Mutter, J. C., 2002, Centered and staggered Fourier derivatives and Hilbert transforms: Geophysics, **67**, 1558-1563.

Dablain, M. A., 1986, The application of high-order differencing to the scalar wave equation: Geophysics, **51**, 54–66.

Fang, K., 1998, Pseudo-spectral modelling of cracked anisotropic media and rotation of multicomponent shear-wave data: M. Sc. Thesis, Univ. of Calgary.

Fornberg, B., 1987, The pseudospectral method - Comparisons with finite differences for the elastic wave equation: Geophysics, **52**, 483-501.

Gaiser, J., 2000, Advantages of 3D P-S-wave data to unravel S-wave birefringence for fracture detection, 70th Ann. Internat. Mtg: Soc. of Expl. Geophys., 1201-1204.

Hill, N. R., 1990, Gaussian beam migration: Geophysics, **55**, 1416–1428.

Holberg, O., 1996, Computational aspects of the choice of operator and sampling interval for numerical differentiation in large-scale simulation of wave phenomena: Geophys. Prosp., **35**, 629–655.

Kosloff, D., and Baysal, E., 1982, Forward modelling by a Fourier method: Geophysics, **47**, 1402-1412.

Lax, P. D., and Wendroff, B., 1964, Difference schemes for hyperbolic equations with high order of accuracy: Comm. Pure Appl. Math., **17**, 381–398.

Li, X.-Y., 1998, Fracture detection using P-P and P-S waves: 68th Annual Internat. Mtg. Soc. Expl. Geoph., Expanded Abstracts, 2056-2059.

Lou, M. and Rial, J.A., 1995, Modelling elastic wave propagation in inhomogeneous anisotropic media by the pseudo spectral method: Geophys. J. Int., **120**, 60-72.

Muir, F., Dellinger, J., Etgen, K., and Nichols, D., 1996, Modelling elastic wavefields across irregular boundaries: Geophysics, **57**, 1189–1193.

Özdenvar, T. and McMechan, G. A., 1996, Causes and reduction of numerical artifacts in pseudo-spectral wavefield extrapolation: Geophys. J. Int., **126**, 819-828.

Ramos-Martinez, J., Ortega, A. A. and McMechan, G. A., 2000, 3D seismic modelling for cracked media: Shear-wave splitting at zero-offset: Geophysics, **65**, 211-221.

Schoenberg. M. and Muir. F., 1989, A calculus for finely layered anisotropic media: Geophysics, **54**: 581-589.

APPENDIX A

NUMERICAL DISPERSION ANALYSIS

Here I describe the analysis of numerical dispersion for the acoustic case. The appropriate equation of motion for an acoustic medium (Kosloff and Baysal, 1982) is:

$$\nabla\left(\frac{1}{\rho}\nabla P\right) = \frac{1}{c^2\rho}\ddot{P} + S \qquad (A1)$$

where P is the pressure, ρ is density, c is the wave velocity and the source term is given in terms of the body force, $\mathbf{f}$, by:

$$S = \frac{1}{\rho}\nabla\cdot\mathbf{f}$$

I consider the case where density is constant (or slowly varying) such that (A1) may be written in the spatial Fourier domain as:

$$-k^2\widetilde{P} = \frac{1}{c^2}\ddot{\widetilde{P}} + \widetilde{S} \qquad (A2)$$

where
$$\widetilde{P}(\mathbf{k},t) = \int_{-\infty}^{\infty}\int_{-\infty}^{\infty}\int_{-\infty}^{\infty} P(\mathbf{x},t)e^{i\mathbf{k}\cdot\mathbf{x}}d^3\mathbf{x}, \qquad \widetilde{S}(\mathbf{k},t) = \int_{-\infty}^{\infty}\int_{-\infty}^{\infty}\int_{-\infty}^{\infty} S(\mathbf{x},t)e^{i\mathbf{k}\cdot\mathbf{x}}d^3\mathbf{x}$$

and
$$k \equiv |\mathbf{k}| = \sqrt{k_x^2 + k_y^2 + k_z^2}$$

As for the elastic case, the second order time derivative is approximated by:

$$\ddot{\widetilde{P}}(\mathbf{k},t) \equiv \frac{\partial^2 \widetilde{P}}{\partial t^2}(\mathbf{k},t) \cong \frac{\widetilde{P}(\mathbf{k},t+\Delta t) - 2\widetilde{P}(\mathbf{k},t) + \widetilde{P}(\mathbf{k},t-\Delta t)}{(\Delta t)^2} \qquad \text{(A3)}$$

Consider the far-field situation for (A2), such that we can ignore the source term, S, and assume a plane wave solution: $\widetilde{P}_1 = e^{i(\mathbf{k}\cdot\mathbf{x}-\omega t)}$. Substitution into (A2), and using the difference approximation (A3) to evaluate the time derivatives, yields:

$$k^2 = \frac{4}{c^2(\Delta t)^2}\sin^2\left(\frac{\omega \Delta t}{2}\right) \qquad \text{(A4)}$$

Thus the actual phase speed of the wave is given by:

$$v(\omega) = \frac{\omega}{k} = \pm\frac{c\omega\Delta t}{2\sin(\omega\Delta t/2)} \qquad \text{(A5)}$$

That the wave propagates dispersively (with a frequency dependent velocity) is a result of the time differencing. An exact evaluation of $\ddot{P}$ in (A2) would give $v = c$, independent of frequency, as expected. The phase velocity as a function of frequency is plotted for two different Δt values in Figure 1, showing the effect of numerical dispersion.

A similar analysis for the 4th order correction yields the following phase speed:

$$v(\omega) = \frac{\omega}{k} = \pm\frac{c\omega\Delta t}{\sqrt{6}}\left\{1 - \sqrt{1 - \frac{4}{3}\sin^2(\omega\Delta t/2)}\right\}^{-1/2}, \qquad \text{(A6)}$$

which suffers considerably less dispersion, for any given Δt, as is seen in Figure 1.

Comparison with finite-difference

Finite-difference methods suffer both temporal and spatial dispersion. For an operator which is second order in time and space, the finite-difference dispersion equation is:

$$\frac{1}{(\Delta x)^2}\sin^2\left(\frac{k\Delta x}{2}\right) = \frac{1}{c^2(\Delta t)^2}\sin^2\left(\frac{\omega\Delta t}{2}\right) \qquad \text{(A7)}$$

At the stability limit, $\Delta x = c\Delta t$, this equation leads to the exact phase velocity:

$$v(\omega) = \frac{\omega}{k} = \pm c \qquad \text{(A8)}$$

Thus there is a "balancing" of numerical dispersion effects in finite-difference modelling of the wave equation, not naturally present in pseudospectral modelling (A4).

A simple correction for simple media

Now let's return to pseudospectral modelling: in cases where the velocity variation is small, an operator designed to compensate for dispersion for a specified velocity could be

used in place of the exact spatial derivative operator, to mimic the balancing observed in finite-difference methods. For example, in the 1D case, the following replacement is used for *k* in the derivative:

$$k \rightarrow \sin(kx_c)/x_c \qquad\qquad (A9)$$

where $x_c \equiv c\Delta t/2$. This substitution is simply made whenever $-ik$ is required to apply a derivative, and entails no extra cost as it is pre-computed. Application of this correction for both the true medium velocity, and a lower velocity is illustrated in Figure A2. This is readily extended to higher dimensions, using radially symmetric versions of (A9).

However, I have found that this correction is less useful for media with large variation in velocities, or for elastic media where both P and S modes are present, since it can only correct for dispersion relating to one propagation velocity. For this reason the fourth order correction described in the main text, with dispersion given by (A6), is preferable.
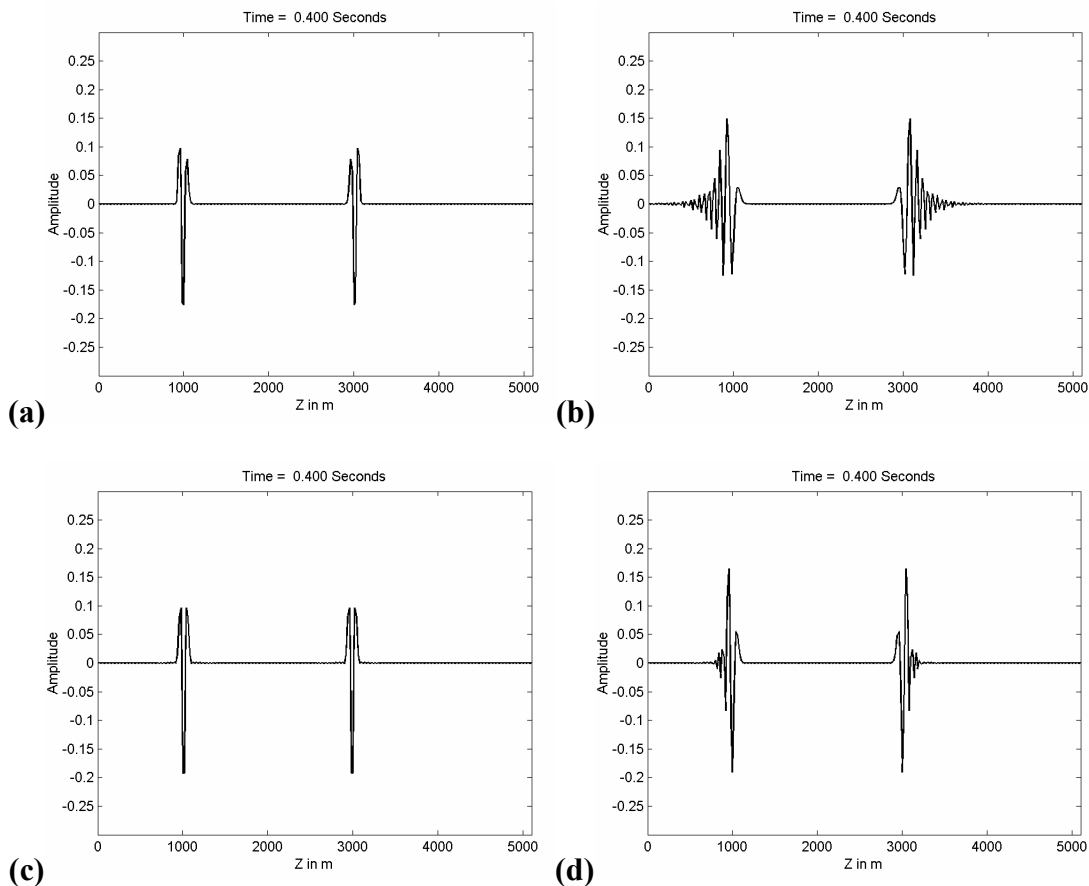

FIG A2: Numerical dispersion in 1D acoustic modelling. The source is located at 2000m, and has a 30Hz zero-phase Ricker wavelet signature. The medium is homogeneous with a velocity of 3000m/sec. The wavefield is shown after 0.4 seconds using: (a) a 1ms time-step; (b) a 4ms time-step with no dispersion correction; (c) a 4ms time-step with dispersion correction for actual medium velocity of 3000 m/sec, and; (d) a 4ms time-step with dispersion correction for 2500 m/sec.

APPENDIX B

ANALYTIC SOLUTION FOR POINT DISLOCATION SOURCE

Aki and Richards (1980, Vol. I., p. 70) give a closed form solution to the elastic wavefield generated by a point dislocation source in a homogeneous isotropic medium. I state this result without proof here.

A point force *S(t)* at the origin with direction $\mathbf{e}_j$ can be written as:

$$\mathbf{f} = S(t)\delta(\mathbf{x})\mathbf{e}_j \tag{B1}$$

where $\mathbf{x}$ is a vector from the origin (i.e. from the source) to the measurement point. Letting $r = |\mathbf{x}|$ be the distance from the source, the displacement at $\mathbf{x}$ is given by:

$$u_i(\mathbf{x},t) = u_i^N + u_i^P + u_i^S \tag{B2a}$$

where the three terms on the right hand side are, respectively: the near field term given by

$$u_i^N = \frac{\left(3\gamma_i\gamma_j - \delta_{ij}\right)}{4\pi\rho r^3} \int\limits_{r/\alpha}^{r/\beta} \tau S(t-\tau)d\tau \; ; \tag{B2b}$$

the P-wave term, given by

$$u_i^P = \frac{\gamma_i\gamma_j}{4\pi\rho\alpha^2 r} S(t - r/\alpha) \; ; \tag{B2c}$$

and the S-wave term, given by

$$u_i^S = \frac{\left(\delta_{ij} - \gamma_i\gamma_j\right)}{4\pi\rho\beta^2 r} S(t - r/\beta) \; . \tag{B2d}$$

Here $\boldsymbol{\gamma}$ is the unit direction vector defined by $\gamma_i = x_i/r$, α and β are the P and S-wave velocities respectively, and ρ is the density of the medium.

Equation (B2) is used to generate the analytical solution of Figure 3 in the main text.